

# We are IntechOpen, the world's leading publisher of Open Access books Built by scientists, for scientists

6,900

Open access books available

185,000

International authors and editors

200M

Downloads

Our authors are among the

154

Countries delivered to

TOP 1%

most cited scientists

12.2%

Contributors from top 500 universities



WEB OF SCIENCE™

Selection of our books indexed in the Book Citation Index  
in Web of Science™ Core Collection (BKCI)

Interested in publishing with us?  
Contact [book.department@intechopen.com](mailto:book.department@intechopen.com)

Numbers displayed above are based on latest data collected.  
For more information visit [www.intechopen.com](http://www.intechopen.com)



# Silicon Nanocrystals and Amorphous Nanoclusters in $\text{SiO}_x$ and $\text{SiN}_x$ : Atomic, Electronic Structure, and Memristor Effects

*Vladimir Volodin, Vladimir Gritsenko,  
Andrei Gismatulin and Albert Chin*

## Abstract

Semiconductor nanocrystals in dielectric films are interesting from fundamental aspect, because quantum-size effects in them appear even at room temperature, so such objects can be called as “quantum dots”. Silicon nanocrystals and amorphous silicon nanoclusters in substoichiometric  $\text{SiO}_x$  and  $\text{SiN}_x$  films are traps for electrons and holes that apply in nonvolatile memory devices. In this chapter the formation of silicon nanocrystals and silicon amorphous nanoclusters in  $\text{SiO}_x$  and  $\text{SiN}_x$  films was studied using structural and optical methods. The phonon confinement model was refined to obtain sizes of silicon nanocrystals from analysis of Raman scattering data. Structural models that lead to nanoscale potential fluctuation in amorphous  $\text{SiO}_x$  and  $\text{SiN}_x$  are considered. A new structural model which is intermediate between random mixture and random bonding models is proposed. Memristor effects in  $\text{SiO}_x$  films are discussed.

**Keywords:** silicon suboxides, silicon subnitrides, nanocrystals, amorphous nanoclusters, phonon confinement model, nanoscale potential fluctuations, memristor

## 1. Introduction

Nanometer-sized semiconductor crystals, the so-called nanocrystals (NCs) and amorphous nanoclusters, embedded in wide-gap insulating matrices, have shown significant promises for application in nanoelectronics (nonvolatile memory) and optoelectronics (light-emitting diodes (LEDs)) [1]. Quantum effects in such hetero-systems are manifested even at room temperature. For example, a bright photoluminescence (PL) was observed in dodecyl-passivated colloidal Si NCs with external quantum efficiency (QE) up to 60% [2]. Since in some experiments single NCs originated delta-function-like energy photoluminescence spectra [3], they can be called as quantum dots. In metal-dielectric-semiconductor structures based on  $\text{SiN}_x$  films with Si nanoclusters, an effective electroluminescence with red, green, and blue light-emitting diodes was demonstrated [4]. Since NCs in a dielectric matrices act also as traps for charge carriers, the NCs' based structures have also

perspectives to yield nonvolatile memory devices [5]. Last time the perspectives of application of nonstoichiometric  $\text{SiO}_x$  and  $\text{SiN}_x$  films with Si NCs and amorphous nanoclusters in memristors have arisen [6]. This chapter is devoted to formation, structural and optical studies of such films, and the development of new structural models which would explain the presence of nanoscale potential fluctuations in such nonstoichiometric films.

## 2. Forming of Si NCs and amorphous nanoclusters in dielectric films

There are several technological approaches for the fabrication of Si NCs and amorphous Si nanoclusters in various dielectric films:  $\text{Si}^+$  ion implantation with consequent thermal annealing; co-sputtering of Si and  $\text{SiO}_2$  targets on cool substrates; chemical vapor deposition (CVD) and plasma-enhanced chemical vapor deposition (PECVD) methods; evaporation of Si, SiO, or  $\text{SiO}_2$  under high vacuum and their deposition onto cool substrates; evaporation of Si target in atmosphere with definite partial pressure of oxygen; and deposition on cool substrates. Each method has advantages and peculiarities.

The main advantage of ion implantation is a very precise control of the dose of the embedded silicon atoms—control of the projected range of silicon ions (it depends on the energy of ions). The disadvantage is the need for high-temperature annealing for the formation of silicon nanoclusters and even more high-temperature annealing (up to  $1150^\circ\text{C}$ ) for their crystallization. So, this process cannot be “back-end-of-line” process in device production.

The benefits of different approaches that use co-sputtering are simplicity, the possibility to control stoichiometry using various intensity of evaporation of the targets, and the opportunity to use different substrates. The CVD and PECVD methods allow using large-scale substrates; the control of stoichiometry is possible using different ratios of reagent gases. The main advantage of PECVD is low temperature of the deposition process, but because almost all reagent gases contain hydrogen, the deposited  $\text{SiO}_x$  and  $\text{SiN}_x$  films are hydrogenated; in this case they should be marked as  $\text{SiO}_x\text{:H}$  and  $\text{SiN}_x\text{:H}$  films. Sometimes the hydrogen content is undesirable because it leads to instability of the characteristics of the films.

It should be noted that applying of various deposition methods leads to variation of the structural model of nonstoichiometric films. The structure of nonstoichiometric  $\text{SiO}_x$  or  $\text{SiN}_x$  films can be described in the framework of the random mixture (RM) or random bonding (RB) models [7]. In the RM model,  $\text{SiO}_x$  is treated as a mixture of two phases: the stoichiometric phase  $\text{SiO}_2$  and the Si. In the RB model,  $\text{SiO}_x$  is assumed to consist of  $\text{Si—O}(\nu)/\text{Si}(4 - \nu)$  structural units,  $\nu = 0, 1, 2, 3$ , or  $4$ , in which Si atoms statistically substitute O atoms in each  $\text{Si—O}(4)$  structural unit. The structure of films formed by ion implantation and co-sputtering with ion beam evaporation of targets is closer to RB model; the structure of PECVD films can be closer to RM model. But structure of real films is always not pure RB or pure RM, and real structure of the films (which is the cause of nanoscale potential fluctuations in nonstoichiometric films) will be discussed below.

## 3. Raman scattering in $\text{SiO}_x$ and $\text{SiN}_x$ films: phonon confinement in Si NCs

Direct methods for studying the structure of nonstoichiometric films (such as high-resolution transmission electron microscopy (HRTEM)) are usually very time-consuming and destructive. Optical methods for studying the structure of NCs

and amorphous nanoclusters are nondestructive and express. Among the optical methods, the most informative is inelastic light scattering—Raman scattering.

Raman scattering measurements are usually carry out to check the presence of a crystalline or amorphous Si phase in as-deposited and annealed SiO<sub>x</sub> and SiN<sub>x</sub> films. Due to the absence of long-range order and breaking of translation symmetry, the Raman spectrum of amorphous Si is an image of effective density of vibrational states for transversal optical (TO) and transversal acoustical (TA) modes and contains two broad peaks at approximately 480 and 150 cm<sup>-1</sup>, correspondingly [8]. According to the quasi-momentum selection rules, in monocrystalline silicon, only phonons from the center of the Brillouin zone are active in Raman scattering; therefore the frequency of the Raman peak in this case is 520.5 cm<sup>-1</sup> [9], and the full width on half maximum (FWHM) usually is about 5 cm<sup>-1</sup>; it is much narrower than the width of amorphous peak. The intensity of the crystalline peak depends on the contents of the crystalline phase, and, using the analysis of experimentally measured integrated Raman scattering intensities  $I_c$  and  $I_a$  for c-Si and a-Si phases, one can obtain the volume part of crystalline phase in a two-phase film. The critical parameter of this method is the ratio of the integrated Raman cross section for c-Si to a-Si,  $\gamma = \Sigma_c/\Sigma_a$ . Knowing this parameter, one can use the next equation:

$$\rho_c = I_c / (I_c + \gamma I_a) \quad (1)$$

Recently, we have clarified the Bustarret data [10] on the dependence of the parameter  $\gamma$  on the size of nano- and micro silicon crystals [11].

Due to softening of the conservation law of quasi-momentum in NCs, the short-wave phonons can take part in Raman scattering in this case. The confined in NCs phonons are characterized by a narrow peak at a position of 500–520 cm<sup>-1</sup>. The position and the width of the peak strongly depend on the size and structure of the NCs [12, 13]. We have developed an improved phonon confinement model (PCM) for the analysis of average size of Si NCs from Raman data.

PCM allows us to calculate the Raman spectra for NCs of various sizes [12–14]. The physical entity of the model is the following. The eigenfunction of phonon with quasi-momentum  $\hbar\mathbf{q}_0$  in an infinite crystal is

$$\Phi(\mathbf{q}_0, \mathbf{r}) = u(\mathbf{r}) e^{i\mathbf{q}_0 \mathbf{r}}, \quad (2)$$

where  $u(\mathbf{r})$  has the periodicity of the lattice and  $\mathbf{q}_0$  is the wavenumber of phonon.

The eigenfunction  $\Psi(\mathbf{q}_0, \mathbf{r})$  for a phonon confined in NCs is a function  $\Phi(\mathbf{q}_0, \mathbf{r})$  multiplied by the phonon weighting function  $W(\mathbf{r}, L)$  (“envelope” function for displacement of atoms in NCs); the weighting function depends on NC size  $L$ :

$$\Psi(\mathbf{q}_0, \mathbf{r}) = W(\mathbf{r}, L)\Phi(\mathbf{q}_0, \mathbf{r}) = \Psi'(\mathbf{q}_0, \mathbf{r})u(\mathbf{r}), \quad (3)$$

where  $\Psi'(\mathbf{q}_0, \mathbf{r})$  is equal to  $W(\mathbf{r}, L) e^{i\mathbf{q}_0 \mathbf{r}}$ . The confined phonon can be described by a wave packet. To calculate the Raman spectrum, one should expand  $\Psi'(\mathbf{q}_0, \mathbf{r})$  in a Fourier presentation:

$$\Psi'(\mathbf{q}_0, \mathbf{r}) = \int C(\mathbf{q}_0, \mathbf{q}) e^{i\mathbf{q} \mathbf{r}} d^3\mathbf{q}. \quad (4)$$

The main task is the determination of Fourier coefficients  $C(\mathbf{q}_0, \mathbf{q})$  from an adequate physical model. The “weight” of the phonon with quasi-momentum  $\hbar\mathbf{q}$  in the wave packet is proportional to  $|C(\mathbf{q}_0, \mathbf{q})|^2$ .

The wavenumber of scattered photon is in our case about three orders of magnitude lower than the wavenumber of a phonon at the Brillouin zone boundary, so one can assume  $\mathbf{q}_0 \cong 0$ . So, the first-order Raman spectrum is

$$I(\omega) \cong \int |C(0, \mathbf{q})|^2 \frac{n(\omega'(\mathbf{q})) + 1}{(\omega - \omega'(\mathbf{q}))^2 + (\Gamma/2)^2} d^3\mathbf{q} \quad (5)$$

where  $n(\omega'(\mathbf{q})) + 1 = \frac{1}{e^{\hbar\omega'(\mathbf{q})/kT} - 1} + 1$  is the Bose-Einstein factor,  $\omega'(\mathbf{q})$  is phonon dispersion, and  $\Gamma$  is FWHM of the Raman peak of a single phonon [12–14]. We also have taken into account that the vibration modes (phonons) with lower frequencies have higher amplitudes of vibration. Energy of vibration  $\hbar\omega'$  is proportional to  $\langle u^2 \rangle k$ , where  $\langle u^2 \rangle$  is standard deviation of an atom from equilibrium position  $k$  which is Hooke's coefficient for a bond, and  $k = m\omega'^2$  ( $m$  is mass of an atom). So, one can derive  $\langle u^2 \rangle \sim \hbar/\omega'$  (Eq. (2.26) in book [15]). This correction is substantial especially for phonons with large frequency dispersion, so we use the equation

$$I(\omega) \cong \int_0^1 |C(0, \mathbf{q})|^2 \frac{n(\omega'(\mathbf{q})) + 1}{\omega'(\mathbf{q}) \cdot ((\omega - \omega'(\mathbf{q}))^2 + (\Gamma/2)^2)} d^3\mathbf{q} \quad (6)$$

It was shown [14] that using a Gaussian curve as eigenfunction for a confined phonon leads to more adequate results than experimental spectra.

Usually, it can be assumed that NCs have a spherical shape with diameter  $L$ . Therefore, in spherical coordinate system, the phonon weighting function  $W(\mathbf{r}, L)$  depends only on radius coordinate  $r$  and does not depend on angles. Assuming that at the boundary of NC ( $r = L/2$ ) the phonon amplitude is equal to  $1/e$  (the phonon amplitude at center of NC is equal to 1), one can obtain.

$$W(\mathbf{r}, L) = \exp(-4r^2/L^2), \text{ so } C(0, \mathbf{q}) \cong \exp\left(-\frac{|\mathbf{q}|^2 L^2}{16}\right) |C(0, q)|^2 \cong \exp\left(-\frac{q^2 L^2}{8}\right) \quad (7)$$

Usually, only empirical expressions for phonon dispersion were used in PCM [12, 13]. But the empirical expressions are accurate enough only near the Brillouin zone center. Also, in earlier approaches, the differences between dispersions of longitudinal optic (LO) and transverse optic (TO) phonons were usually not taken into account. In general, for crystals with diamond-type lattice, there are six phonon branches with dispersions  $\omega_i'(q)$ , so the first-order Raman spectrum for phonon weighting function  $W(\mathbf{r}, L) = \exp(-4r^2/L^2)$  is

$$I(\omega) \cong \sum_{i=1}^6 \int_0^{q_{\max}} \exp\left(-\frac{q^2 L^2}{8}\right) \frac{n(\omega_i'(q)) + 1}{\omega_i'(q) \cdot ((\omega - \omega_i'(q))^2 + (\Gamma/2)^2)} q^2 dq. \quad (8)$$

Wavenumbers are varied from 0 up to  $q_{\max}$  (edge of the Brillouin zone). For directions with high symmetry ( $\langle 100 \rangle$  and  $\langle 111 \rangle$ ), it should be noted that some phonon branches are degenerated. The density of states for phonons is proportional to  $q^2 dq$ .

In some approaches, the phonon frequencies are determined using “ab initio” quantum mechanical calculations [16], but this method requires large computational resources, while NCs with diameters  $> 3$  nm contain more than 1 thousand atoms. So, for calculation of phonon dispersion, the Keating model of



valence forces [17] was used. In this simple but adequate model, the elastic energy of the crystal depends on bond length and on deviation of bond angle from ideal tetrahedral angles. We consider atom-atom interaction only between the nearest neighbor. For a crystal with diamond-type lattice, the elastic energy of unit cell is

$$E = \frac{3}{16} \sum_i \sum_j \frac{k_l}{a^2} \left( (\vec{r}_i - \vec{r}_j)^2 - \frac{3a^2}{16} \right)^2 + \frac{3}{8} \sum_i \sum_{k,j>k} \frac{k_\phi}{a^2} \left( (\vec{r}_i - \vec{r}_j) \cdot (\vec{r}_i - \vec{r}_k) + \frac{a^2}{16} \right)^2, \quad (9)$$

where  $k_l$  and  $k_\phi$  are elastic constants (Hooke's coefficients) and  $a$  is lattice constant. TO and LO phonons at the Brillouin zone center are degenerated for crystals with diamond-type lattice. The frequency is given by

$$\omega_T = \sqrt{\frac{8(k_l + 3k_\phi)}{3m}} \quad (10)$$

where  $m$  is the mass of Ge atoms. As it was mentioned above, Si frequency of TO and LO phonons at the Brillouin zone center is equal to  $520.5 \text{ cm}^{-1}$ . So, the elastic constants  $k_\phi$  and  $k_l$  are not independent [see Eq. (10)]. The elastic constant  $k_l$  was determined from approximation of calculated dispersions in directions  $\langle 100 \rangle$ ,  $\langle 110 \rangle$ , and  $\langle 111 \rangle$ , obtained from neutron scattering data [18, 19]. It is important to consider phonons of different directions, because in experiment, Raman signal comes from a large amount of randomly oriented NCs, and all phonon modes are intermixed. The exact expressions for phonon dispersions in directions  $\langle 100 \rangle$ ,  $\langle 110 \rangle$ , and  $\langle 111 \rangle$  for Keating model are published in Ref. [14] and are very cumbersome. To calculate the first-order Raman spectrum, one should use these dispersions in the Eq. (8). Dispersion in different directions should be used with its corresponding weight. There are 6 physically equivalent  $\langle 100 \rangle$  directions, so the weight of this dispersion is 6. Similarly the weight of dispersion along  $\langle 111 \rangle$  and  $\langle 110 \rangle$  directions are, respectively, equal to 8 and 12. Thus, all calculations were performed with the phonon dispersion in the Keating model, taking into account the phonon dispersion for the three main directions in Si.

**Figure 1** shows the results of calculations of the Raman spectra of Si NCs of different diameters using improved PCM. It is seen that for Si NC with diameter of 10 nm, the effect of phonon confinement is significant. The peak shifted and broadened relative to the peak from the bulk Si. For sizes below 10 nm, the NCs' Raman spectrum becomes asymmetric.

**Figures 2** and **3** summarize the results of calculations compared with experimental results. **Figure 2** shows the difference between the position of Raman peaks of Si NCs and bulk Si. The average sizes of the Si NCs were determined from HRTEM data. As can be seen, the results of calculations in improved PCM agree well with experimental data but have some differences from the simulation results presented in earlier works [12, 13, 16]. It should be noted that results of calculations in the improved PCM are adequate for a broad range of Si NCs' sizes (from 3 to 10 nm). Note, however, that if during measurements, the heating of the sample under laser spot takes place, the Raman peak will shift (due to anharmonicity of phonons). If the system contains mechanical stress, it will also cause a shift of the Raman peak [14]. **Figure 3** shows the dependence of the Raman peak width with the size of the NCs, for calculation with improved PCM and for experimental data. Some differences between the experimental data and calculations are visible. In particular, large width of the experimental spectra, compared with the calculated spectra, may be due to the dispersion of the size of the Si NCs. Thus, if anharmonicity effect due to heating or mechanical stress is not relevant, the present

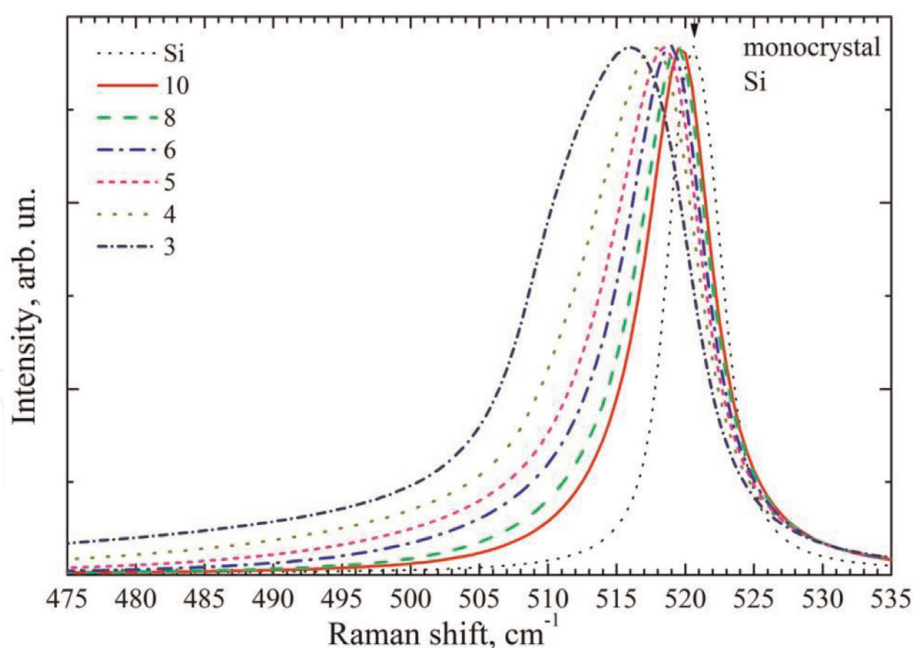


**Figure 1.**  
Calculated Raman spectra of Si NCs of diameters from 10 to 3 nm.

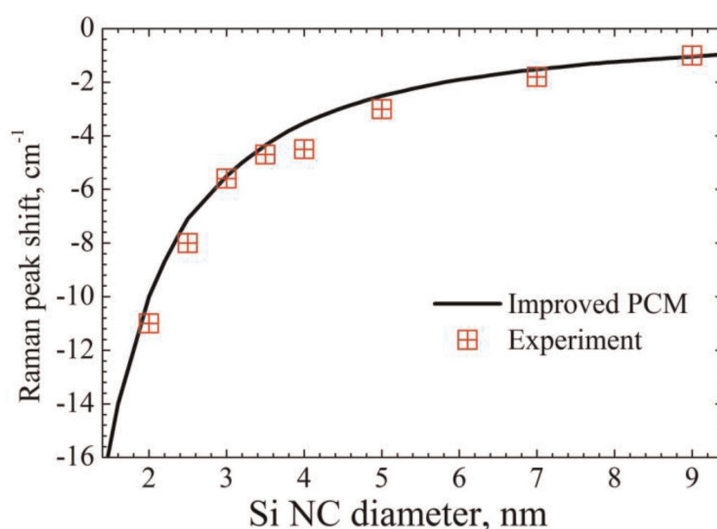


**Figure 2.**  
Shift of the position of the Raman peak for optical phonons confined in Si NCs of various sizes is shown relative to position of Raman peak for bulk Si. The solid curve represents the results obtained using improved PCM (dispersion is calculated in the Keating model taking into account the angular phonon dispersion); red crosses show the experimental data.

improved model allows us to determine the average size of the Si NCs from the analysis of the Raman spectra for a wide range of sizes.

Experimental data on **Figures 2 and 3** were obtained for Si NCs in  $\text{SiO}_x$ ,  $\text{SiN}_x$ , and amorphous Si matrix and also for free-standing Si nanopowders. This indicates that the PCM is adequate for various matrices; the main demand is that localized phonons in NCs strongly damp in matrix.

In **Figure 4** the Raman spectra of PECVD-deposited  $\text{SiO}_x\text{:H}$  films are shown. Deposition was made from the mixture of monosilane ( $\text{SiH}_4$ ) diluted by argon (Ar) and oxygen ( $\text{O}_2$ ) diluted by helium (He). The stoichiometry parameter “x” was changed by varying of oxygen concentration. The temperature of Si (100) monocrystalline substrate was 200°C. The thickness of  $\text{SiO}_x\text{:H}$  films was about 200 nm. The value of stoichiometry parameter “x” was obtained from the analysis of X-ray photoelectron spectroscopy (XPS) data.

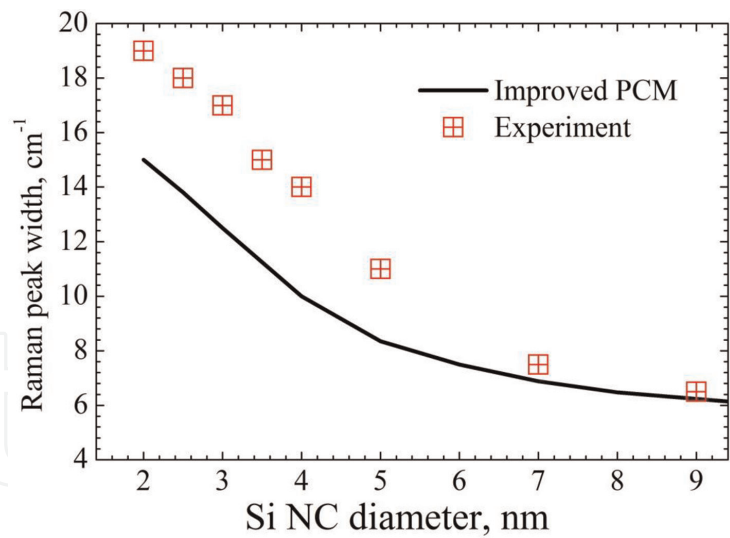


**Figure 3.** Width of the Raman peak for optical phonons confined in Si NCs of various sizes. The solid curve represents the results of calculation; red crosses show the experimental data.

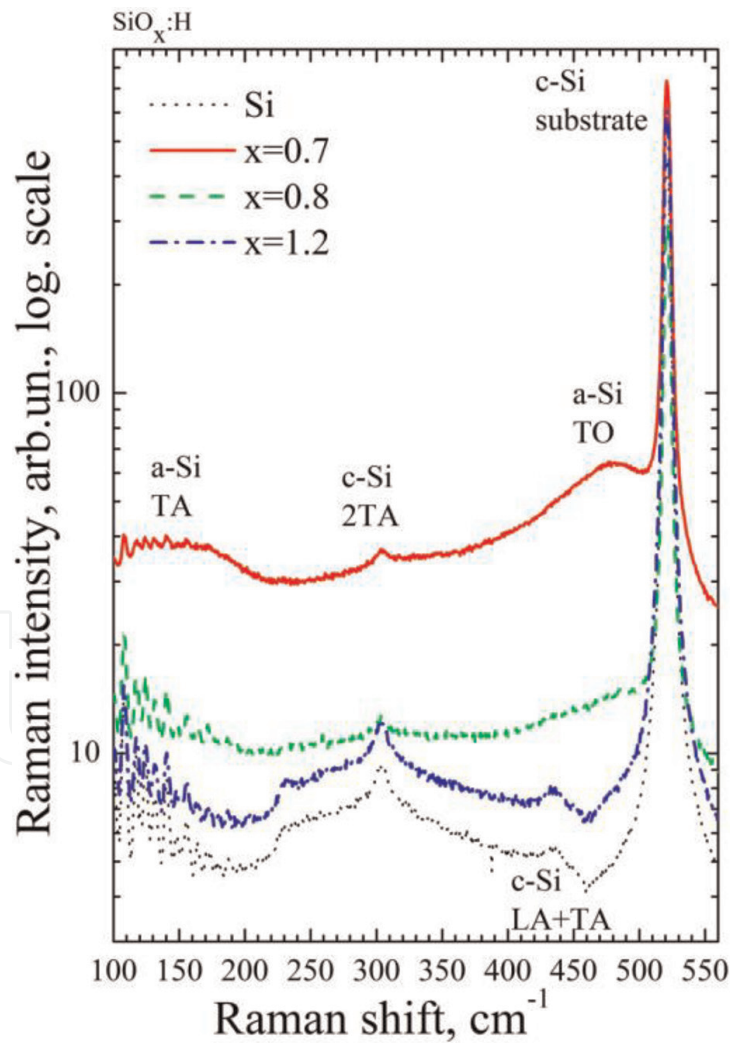


**Figure 4.** Raman spectra of  $\text{SiO}_x\text{:H}$  films of different stoichiometry.

Raman spectra were registered at room temperature in back-scattering geometry. For excitation, the 514.5-nm line of an  $\text{Ar}^+$  laser was used. No polarization analysis for scattered light was performed. A Horiba Jobin Yvon T64000 spectrometer was used for measuring Raman spectra with a spectral resolution better



than  $2\text{ cm}^{-1}$ . A special facility for microscopic Raman studies was also employed. The laser-beam power reaching the sample was 2 mW. For minimization of the heating of the structures under the laser beam, the sample was placed somewhat below the focus in a situation in which the laser-spot size was equal to  $10\text{ }\mu\text{m}$ .

So, registered Raman spectra of the  $\text{SiO}_x\text{:H}$  films and the Raman spectrum of a monocrystalline silicon substrate are shown in **Figure 4**. Evidently, a very intense signal due to silicon substrate is observed; this is a line due to the  $520.5\text{ cm}^{-1}$  long-wave optical phonon. For clarity, the vertical scale is plotted logarithmic. Besides, features originating from two-phonon scattering phenomena, namely, those due to events involving two acoustic phonons ( $2\text{TA} \sim 300\text{ cm}^{-1}$ ,  $\text{LA} + \text{TA} \sim 425\text{ cm}^{-1}$ ), were observed in the spectrum of single-crystal silicon.  $\text{SiO}_x\text{:H}$  films are semitransparent ones in the visible light, and their spectrum also exhibits a signal due to the substrate. The narrow peaks with wavenumbers lower than  $160\text{ cm}^{-1}$  resulted from the inelastic scattering of light by atmospheric molecules. As it was mentioned, in Raman spectrum of amorphous Si clusters, there are TO ( $480\text{ cm}^{-1}$ )- and TA ( $150\text{ cm}^{-1}$ )-related broad peaks.

In **Figure 4** one can see that the  $\text{SiO}_x\text{:H}$  films with  $x < 1$  contain noticeable amount of amorphous Si clusters. In the spectrum of film with  $x = 1.2$ , the TO and TA peaks are practically absent. If the structure of this film corresponded to the RM model, then a significant number of clusters of amorphous silicon would be present in it.

A similar picture is observed for PECVD-grown  $\text{SiN}_x\text{:H}$  films (**Figure 5a**).

The studied  $\text{SiN}_x\text{:H}$  films of different stoichiometric composition were grown using PECVD from a mixture of ammonia ( $\text{NH}_3$ ) and monosilane ( $\text{SiH}_4$ ) on Si substrates with orientation (001). It is known that the composition of  $\text{SiN}_x$  films ( $0 < x < 4/3$ ) depends on the  $\text{NH}_3/\text{SiH}_4$  flow ratio. The temperature of the substrates during deposition was  $150^\circ\text{C}$ . The value of stoichiometry parameter “x” was defined using of XPS data.

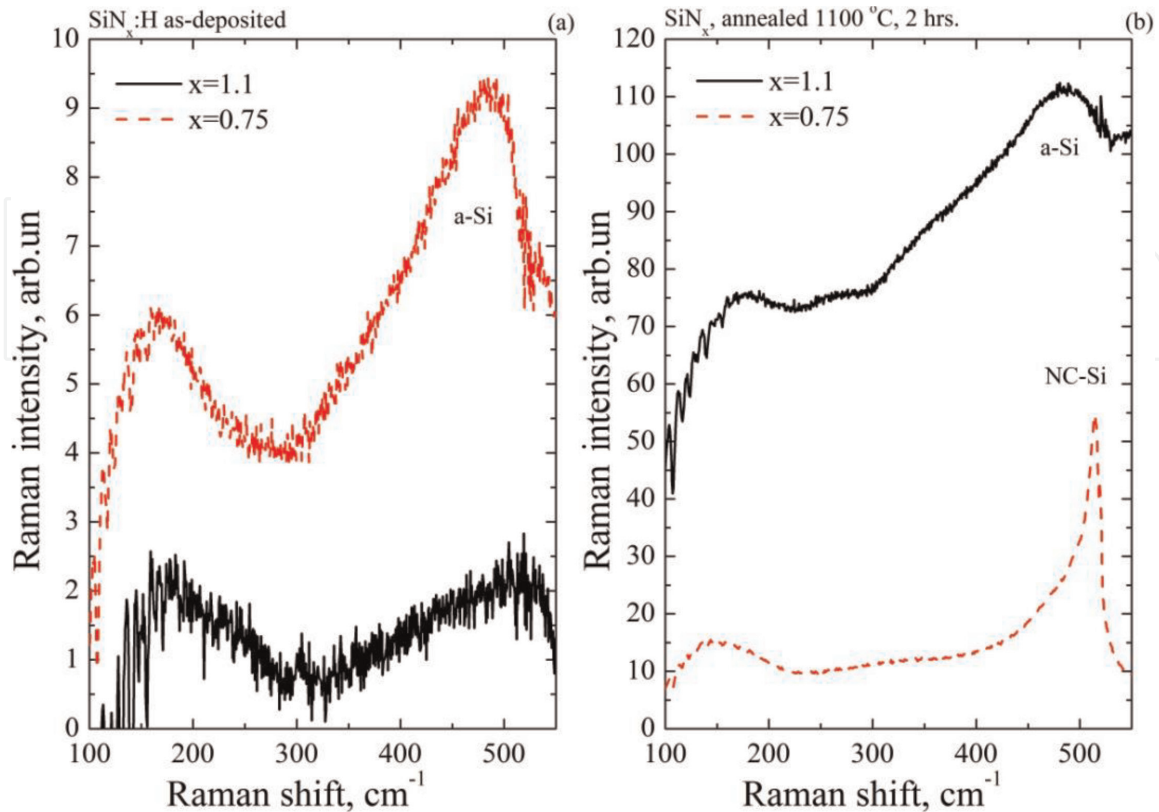


**Figure 5.** Raman spectra of  $\text{SiN}_x\text{:H}$  films of different stoichiometry: (a) as-deposited films and (b) as-annealed films.

One can see in Raman spectra of as-deposited SiN<sub>x</sub>:H films the amorphous Si peaks (**Figure 5a**). It should be noted that the spectrum of Si substrate was subtracted from spectra of studied structures. One can see that the SiN<sub>x</sub>:H films with  $x < 1$  contain noticeable amount of amorphous Si clusters. In the as-deposited sample with  $x = 1.1$ , the signal from amorphous Si is present, but small.

In **Figure 5b** the spectra of SiN<sub>x</sub> films after annealing at Ar atmosphere (1100°C, 2 hours) are presented. One can see that in spectrum of sample with low concentration of Si ( $x = 1.1$ ), the annealing leads to growth of TO and TA peaks related to amorphous Si. It means that the annealing contributed to the gathering of excess silicon atoms into amorphous clusters and the structure of annealed film is close to RM model. Nevertheless, even such a high-temperature annealing did not lead to crystallization of amorphous nanoclusters. In spectrum of SiN<sub>0.75</sub> film, there is narrower peak with position  $514.5 \text{ cm}^{-1}$ . The shift compared with position of peak of monocrystalline Si is about  $6 \text{ cm}^{-1}$ . According to the data presented in **Figure 2**, such shift is corresponding to Raman scattering by optical phonons localized in Si NCs with average size about 3 nm. It is worth to note that this size is closed to critical size of stable crystalline nuclei of Si.

The photoluminescence under excitation with ultraviolet laser HeCd laser ( $\lambda = 325 \text{ nm}$ ) was also studied in as-deposited and annealed SiN<sub>x</sub>:H films. Annealing leads to an increase in the intensity of the photoluminescence, apparently due to the annealing of non-radiative defects. The maximum of the photoluminescence signal shifted to the long-wavelength direction (redshift) with an increase in the content of excess silicon in silicon nitride films.

#### 4. IR absorption in SiO<sub>x</sub> and SiN<sub>x</sub> films: the evidence of deviation from the RM model

The SiO<sub>x</sub>:H and SiN<sub>x</sub>:H films were studied using Fourier transform infrared (FTIR) absorption spectroscopy; the spectrometer FT-801 having a spectral resolution of  $4 \text{ cm}^{-1}$  was used.

The IR spectra of SiO<sub>x</sub> samples in **Figure 6** show an absorption peak on the stretching vibrations of the Si—O bonds (TO<sub>3</sub> peak [20]). Pai et al. [21] found that the position of this peak (in inverse centimeters) in SiO<sub>x</sub> films almost linearly depends on the stoichiometry parameter  $x$ , like.

$$\nu = 925 + 75x \quad (11)$$

From the data of **Figure 6**, it can be seen that the position of the TO<sub>3</sub> peak for the studied samples varies from  $1040$  to  $1060 \text{ cm}^{-1}$ . So, according to Eq. (11), the expected stoichiometry of silicon oxide SiO<sub>x</sub> should change only slightly. But, according to XPS data, the stoichiometry of the SiO<sub>x</sub> films varies widely (from 0.7 to 1.2). This suggests that the structure of our films does not correspond to the RB model (otherwise, the shift range of the TO<sub>3</sub> peak position would be much wider). However, the structure of our films does not correspond to the RM model either (the position of the TO<sub>3</sub> peak for all the films would correspond to the SiO<sub>2</sub> matrix and would be about  $1075 \text{ cm}^{-1}$ ). It is worth also to note that the peaks corresponding to absorption by Si—H and O—H bonds were observed in the films, so the as-deposited SiO<sub>x</sub> films are hydrogenated.

**Figure 7a** shows the IR absorption spectra of as-deposited SiN<sub>x</sub>:H films as well as silicon substrate. Nonpolar Si—Si bonds that are active in the Raman process are not active in the absorption process, but Si—N, Si—H, and N—H bonds are active in it, which makes it possible to obtain information on the structure of a-SiN<sub>x</sub>:H films

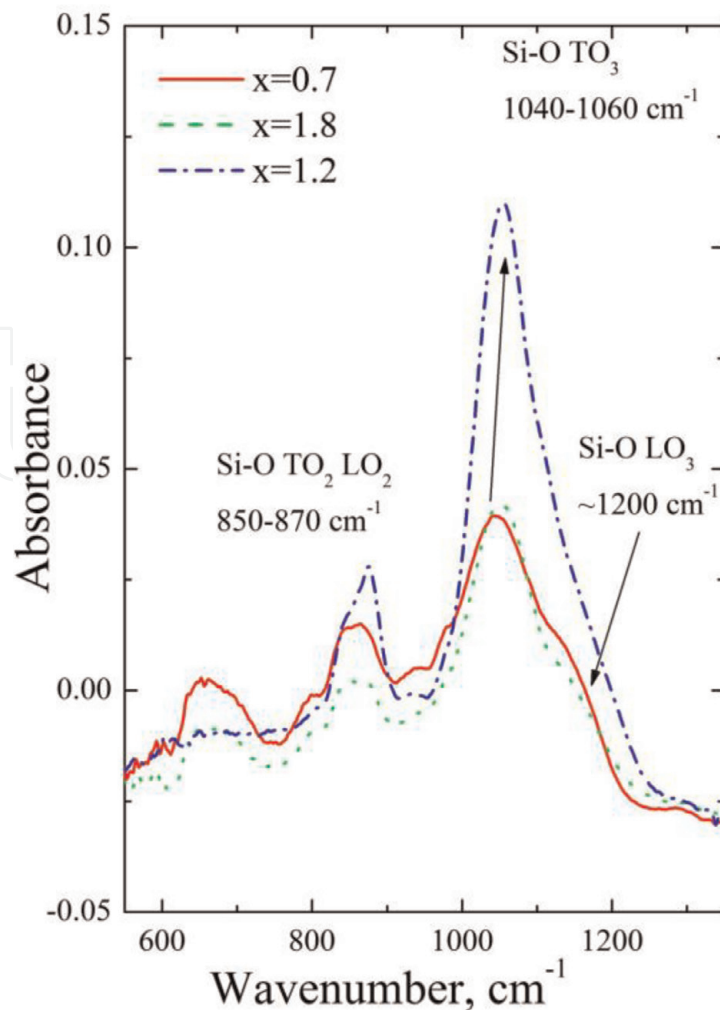


**Figure 6.**  
IR-absorbance spectra of  $\text{SiO}_x\text{:H}$  films of different stoichiometry.

using the IR absorption method. Optical density  $A$  (natural logarithm of  $1/T$ , where  $T$  is transmission) is plotted on the vertical axis. In the spectra of the films grown at high ratio of ammonia to monosilane fluxes ( $x = 1.3$ ), absorption peaks at  $3340\text{ cm}^{-1}$  are visible. This is the absorption on the stretching vibrations of the nitrogen-hydrogen bonds [22]. In the spectra of the films grown at a ratio of ammonia to monosilane fluxes of 1 and 0.5 ( $x = 1.1$  and  $0.75$  accordingly), the intensity of this peak is very low, which means that the concentration of hydrogen bound to nitrogen decreases with increasing concentration of excess silicon. It is also seen from **Figure 7** that the spectra of samples containing excess silicon contain a peak with a position of  $2150\text{ cm}^{-1}$ . This is the peak from absorption on the stretching vibrations of the silicon-hydrogen bonds [22]. The intensity of this peak depends on the ammonia/monosilane ratio; the intensity is very low in  $\text{Si}_3\text{N}_4$  film, but it grows with increasing concentration of excess silicon. The peak at  $\sim 1100\text{ cm}^{-1}$  observed in all spectra corresponds to the absorption of stretching vibrations of silicon-oxygen bonds in the silicon substrate. These bonds also give peaks from  $400$  to  $800\text{ cm}^{-1}$  of twisting, wagging, rocking, and scissor modes. In addition, the spectrum of monocrystalline silicon contains peaks from multiphonon lattice absorption in silicon itself (features in the region of  $607\text{--}614\text{ cm}^{-1}$ ). In some spectra, there is also a “parasitic” peak with a position of  $2350\text{--}2400\text{ cm}^{-1}$  associated with absorption on carbon dioxide gas (in the process of measuring its concentration slightly changed, as a result it was not completely

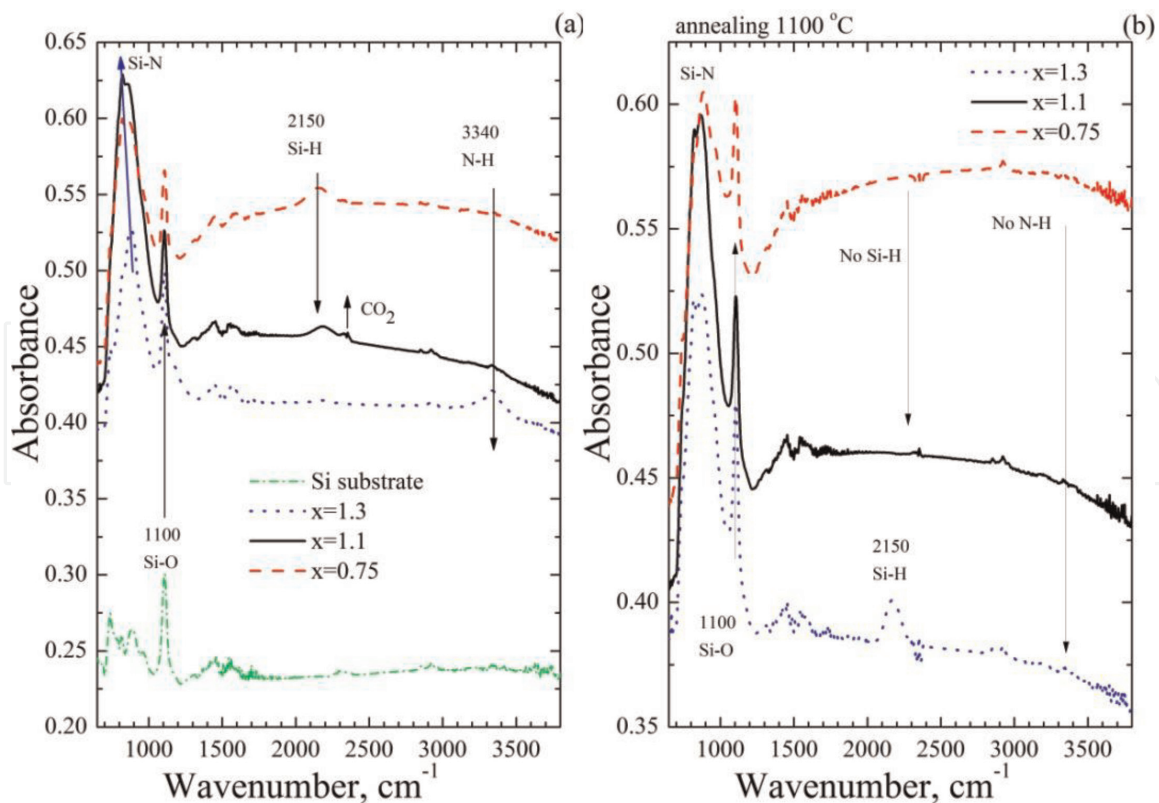


**Figure 7.**  
 IR-absorbance spectra of  $\text{SiN}_x\text{:H}$  films of different stoichiometry: (a) as-deposited films and (b) as-annealed films.

removed when dividing the spectrum from the samples by the reference spectrum of the air).

Let us turn to the absorption peak due to vibrations of the Si—N bonds in **Figure 7**. In the spectra of all the films, there are peaks from the stretching vibrations of these bonds. The spectra were approximated by Gaussian curves, and peak positions were determined. The position of the absorption peaks on the stretching vibrations of the Si—N bonds is shifted, depending on the stoichiometry, from 880 to 860  $\text{cm}^{-1}$ . This effect was previously known (see work [23] and references therein). The general dependence is that the oscillation frequency decreases with decreasing stoichiometric parameter  $x$  in a  $\text{SiN}_x$  film. This is observed in our experiment and again confirms that the structure of the films cannot be considered only within the framework of the RM model (in which the stoichiometry of the matrix surrounding the silicon inclusions is unchanged—the matrix parameter  $x$  is 4/3).

**Figure 7b** shows the IR absorption spectra of annealed (Ar atmosphere, 1100°C, 2 hours)  $\text{SiN}_x\text{:H}$  films. One can see that annealing leads to evaporation of hydrogen, except nearly stoichiometry ( $x = 1.3$ ) film. In that film the Si—H peak becomes even more intensive after annealing. So, hydrogen has been removed from N—H bonds to Si—H bonds. This effect has already been observed in the work [24]. In the work [24], it was shown that in order to remove hydrogen from Si—H bonds, it is necessary to apply high-temperature annealing at very high pressure. It should be noted that in annealed films the position of the absorption peaks on the stretching vibrations of the Si—N bonds is also shifted, depending on the stoichiometry. The lesser parameter  $x$ , the higher is frequency of stretching vibrations of the Si—N bonds.



So, the analysis of IR absorption data is an evidence of deviation of structure of real  $\text{SiO}_x$  and  $\text{SiN}_x$  films from the RM model.

## 5. New structural model explaining nanofluctuations of potential in $\text{SiO}_x$ and $\text{SiN}_x$

Nonstoichiometric silicon oxide  $\text{SiO}_x$  and nitride  $\text{SiN}_x$  are tetrahedral compounds whose structure is defined by the Mott octahedral rule [7, 25].  $\text{SiO}_x$  and  $\text{SiN}_x$  are synthesized under thermodynamically nonequilibrium conditions. Therefore, the structure of nonstoichiometric  $\text{SiO}_x$  and  $\text{SiN}_x$  layers depends on synthesis conditions, i.e., temperatures, gas pressure, and annealing.

The RB and RM models [7] are two extreme cases of the  $\text{SiO}_x$  and  $\text{SiN}_x$  structure description. As a rule, at low synthesis temperatures ( $<300^\circ\text{C}$ ), its structure is described by the RB model; higher synthesis temperatures promote phase separation in  $\text{SiO}_x$  layers, i.e., such layers should be better described by the RM model.

According to the RB model [26], the probability of finding the  $\text{SiO}_v\text{Si}_{(4-v)}$  tetrahedron (the fraction of given  $v$ -type tetrahedra), where  $v = 0, 1, 2, 3, 4$  in  $\text{SiO}_x$  for composition  $x$ , is given by.

$$W_\nu^{RB}(x) = \frac{4!}{\nu!(4-\nu)!} \left(\frac{x}{2}\right)^\nu \left(1 - \frac{x}{2}\right)^{4-\nu} \quad (12)$$

According to the RM model [7], the calculated spectrum consists of two tetrahedron types,  $\text{SiO}_4$  and  $\text{SiSi}_4$ . The fraction of  $\text{SiO}_4$  and  $\text{SiSi}_4$  tetrahedra in the calculation of Si 2p spectra is  $(1 - x/2)$  and  $x/2$ , respectively. To simulate the photoelectron spectrum  $I(E)$ , the  $W_\nu$  peaks obtained using the RB and RM models were broadened by the Gaussian using the formula:

$$I(E) = \sum_\nu W_\nu e^{-(E-E_\nu)^2/2\sigma_\nu^2} \quad (13)$$

where  $E_\nu$  and  $\sigma_\nu$  are the peak energy and “half-width” for a given tetrahedron type. The  $\text{SiO}_x$  film composition was calculated assuming that the calculated spectrum is a superposition of five peaks corresponding to five  $\text{SiO}_v\text{Si}_{(4-v)}$  tetrahedra,  $v = 0, 1, 2, 3, 4$ . The fraction of tetrahedral was selected from the best fit of the spectrum  $I(E)$  calculated by Formula (12).

**Figure 8a** shows five experimental photoelectron spectra of the Si 2p level in  $\text{SiO}_x$ . We can see that the energy and half-width of the  $\text{Si}_{4+}$  peak belonging to the  $\alpha\text{-SiO}_2$  phase and the Si peak belonging to the  $\alpha\text{-Si}$  phase are  $E_0 = 103.5$  eV and  $\sigma_0 = 1.2$  eV and  $E_4 = 99.5$  eV and  $\sigma_4 = 0.6$  eV, respectively. The position and half-width for  $\text{Si}_{3+}$ ,  $\text{Si}_{2+}$ , and  $\text{Si}_{1+}$  peaks ( $\text{SiSiO}_3$ ,  $\text{SiSi}_2\text{O}_2$ , and  $\text{SiSi}_3\text{O}$  tetrahedra) were determined using linear interpolation of  $E_0$ ,  $E_4$ ,  $\sigma_0$ , and  $\sigma_4$  using the number of oxygen atoms as a parameter. Dashed curves in **Figure 8a** show the spectra calculated from the best fit with experimental spectra. The calculation for the  $\text{SiO}_x$  film composition predicts the following values,  $x = 0, 0.7, 0.98, 1.47$ , and  $2.0$ .

**Figure 8b** shows the experimental photoelectron spectra of the Si 2p level in  $\text{SiO}_x$  and the results of RB model simulation. The RB model predicts a single peak being a superposition of five peaks corresponding to five  $\text{SiO}_v\text{Si}_{(4-v)}$  tetrahedra ( $v = 0, 1, 2, 3, 4$ ). The calculated peak shifts to lower binding energies with decreasing oxygen concentrations. The position and half-width of the calculated  $\text{SiO}_x$  peak for  $x = 0.7, 0.98, 1.47$  is not in agreement with the experimental spectrum

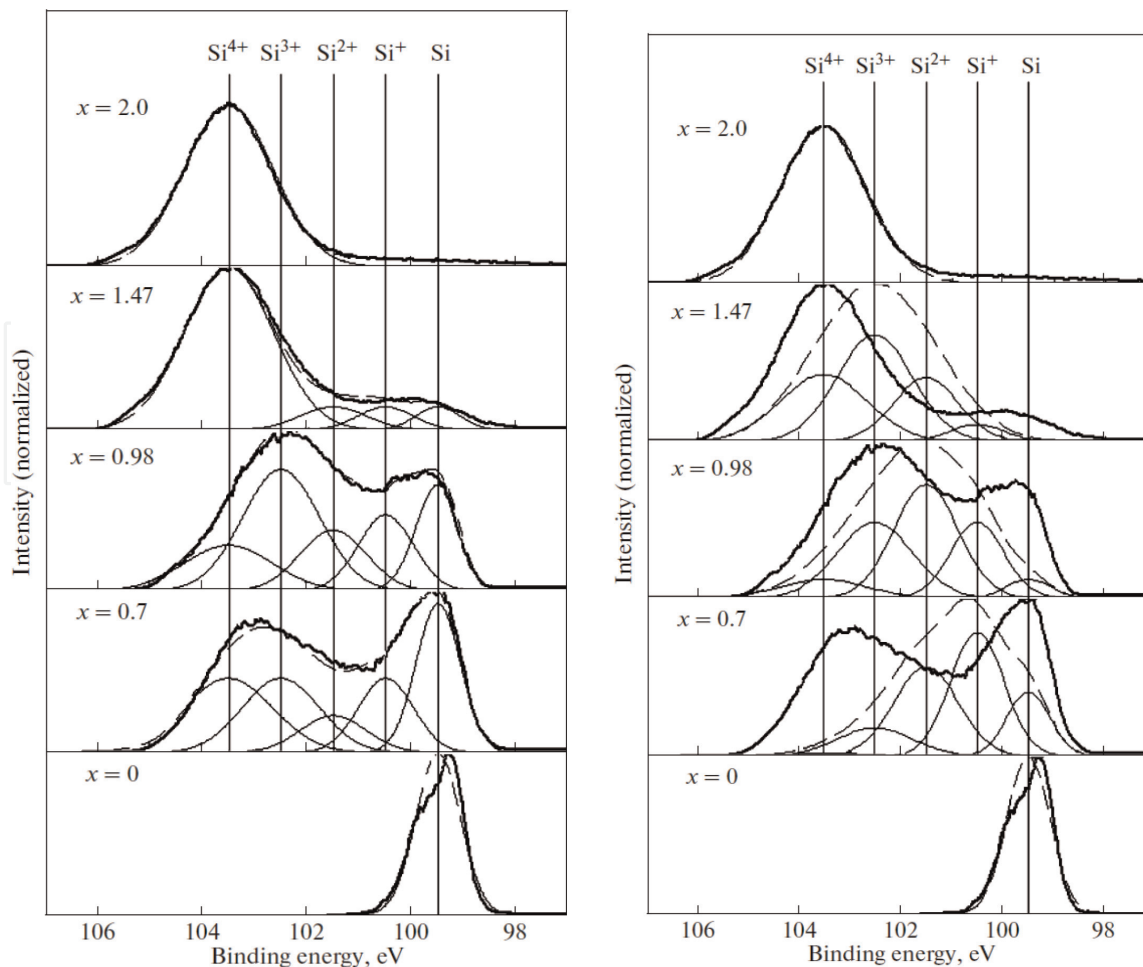


**Figure 8.** (a) (left) Experimental photoelectron spectra of the Si 2p level in  $\text{SiO}_x$  (bold curve) and simulation results for determining the film composition (dashed curve). Symbols  $\text{Si}_4^+$ ,  $\text{Si}_3^+$ ,  $\text{Si}_2^+$ ,  $\text{Si}^+$ , and  $\text{Si}$  indicate intensities of the Si 2p level for  $\text{SiO}_4$ ,  $\text{SiSiO}_3$ ,  $\text{SiSi}_2\text{O}_2$ ,  $\text{SiSi}_3\text{O}$ , and  $\text{SiSi}_4$  tetrahedra, respectively. (b) (right) Experimental photoelectron spectra of the Si 2p level in  $\text{SiO}_x$  (bold curve) and the results of simulation using the RB model (dashed curve). Symbols  $\text{Si}_4^+$ ,  $\text{Si}_3^+$ ,  $\text{Si}_2^+$ ,  $\text{Si}^+$ , and  $\text{Si}$  indicate intensities of the Si 2p level for  $\text{SiO}_4$ ,  $\text{SiSiO}_3$ ,  $\text{SiSi}_2\text{O}_2$ ,  $\text{SiSi}_3\text{O}$ , and  $\text{SiSi}_4$  tetrahedra, respectively.

of the Si 2p level. The RB model underestimates the role of  $\text{SiSi}_4$  and  $\text{SiO}_4$  tetrahedra in calculating the intermediate  $\text{SiO}_x$  composition ( $x = 0.7, 0.98, 1.47$ ). Thus, there are five  $\text{SiO}_v\text{Si}_{(4-v)}$  tetrahedron types in  $\text{SiO}_x$ ; however, the probability of their detection is not quantitatively described by the RB model.

The calculation of experimental spectra using the RM model is shown in **Figure 9a**. According to the RM model, the calculation predicts the existence of two peaks corresponding to  $\text{SiO}_4$  and  $\text{SiSi}_4$  tetrahedra. The calculated energies of the Si 2p level peaks correlate with those of experimental spectra. The calculated spectra underestimate the contribution of  $\text{SiSiO}_3$ ,  $\text{SiSi}_2\text{O}_2$ , and  $\text{SiSi}_3\text{O}$  tetrahedra which exist in experimental spectra. For example, for  $\text{SiO}_{0.98}$ , the calculation predicts the presence of the  $\text{SiO}_2$  phase which is not observed in experimental spectra. Thus, the RM model also does not describe the experimental photoelectron spectra.

We note that it is impossible to describe experimental spectra by summing the RB and RM spectra in corresponding proportions. This is easily seen in the case of the composition  $x = 0.7$  for which both RB and RM models predict a significantly smaller content of the  $\text{SiO}_2$  phase than it is observed in the experiment.

**Figure 9b** shows the photoelectron spectra of the valence band of  $\text{SiO}_x$  of variable composition, measured at an excitation energy of 1486.6 eV. At such an excitation energy, silicon states make the main contribution to the valence band

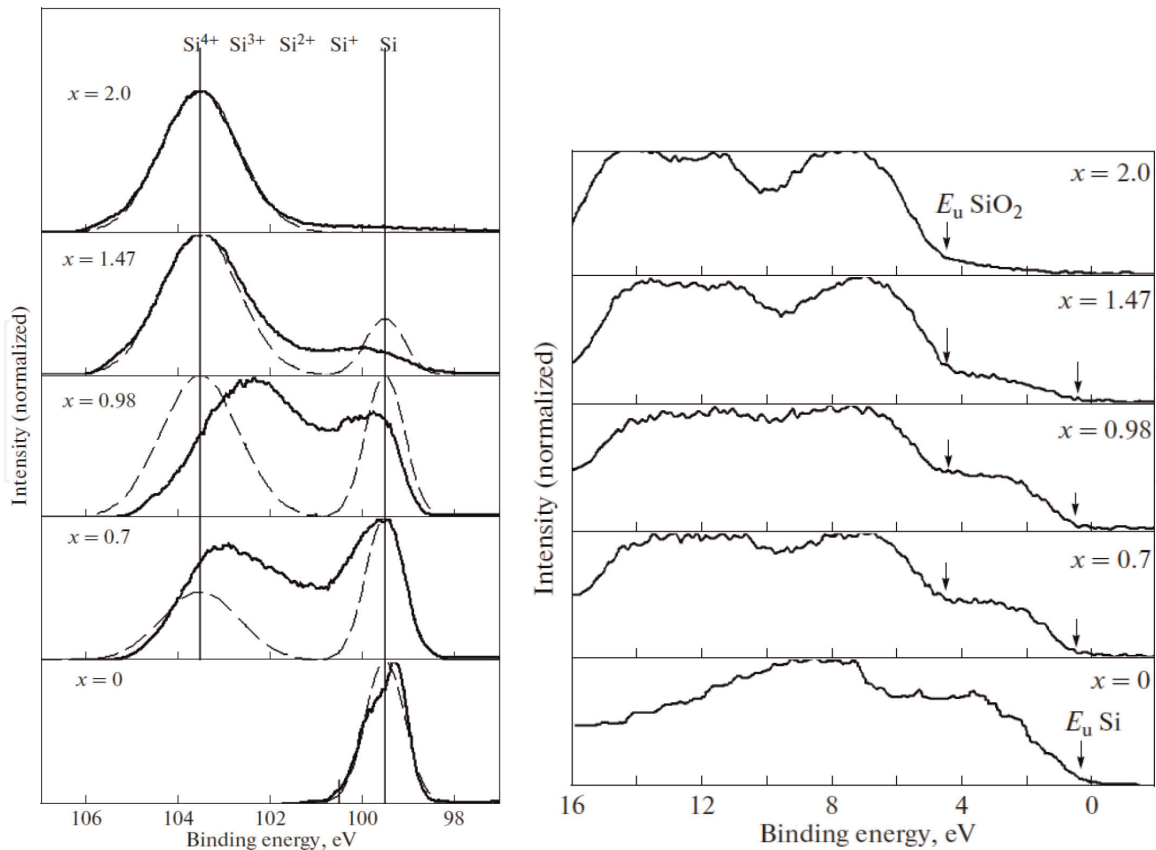


**Figure 9.**

(a) (left) Experimental photoelectron spectra of the Si 2p level in  $\text{SiO}_x$  (bold curve) and the results of simulation using the RM model (dashed curve). Symbols  $\text{Si}^{4+}$  and  $\text{Si}$  indicate intensities of the Si 2p level for  $\text{SiO}_4$  and  $\text{SiSi}_4$  tetrahedra, respectively. (b) (right) Experimental XPS data of the valence band of  $\text{SiO}_2$ ,  $\text{SiO}_x$ , and Si. The top of the silicon valence band is taken as the reference point.

spectrum. Oxygen states (O 2p) at such excitation energies make a small contribution due to a low photoionization cross section. The  $\text{SiO}_x$  ( $x > 0$ ) photoelectron spectrum contains three distinct peaks. As the silicon contents in  $\text{SiO}_x$  increase above the top of the silicon valence band ( $E_v$  Si), states caused by silicon appear (**Figure 9b**). The low-energy peak at 0–4 eV is caused by Si 3p orbitals in amorphous silicon. The peaks at energies above 4 eV are caused by Si 3s and 3p orbitals. These results independently point to the fact that  $\text{SiO}_x$  contains  $\text{SiO}_2$  and Si.

To describe the  $\text{SiO}_x$  structure, it was proposed to use the intermediate model (IM). The IM model assumes local fluctuations of the  $\text{SiO}_x$  chemical composition, which result in bandgap fluctuations. For example, in [27], it was shown that the chemical composition of silicon oxide films can be identical,  $\text{SiO}_{1.94}$ , while the bandgap can vary in the range of 5.0–7.5 eV. **Figure 10a** shows the  $\text{SiO}_x$  energy-level diagram for section A–A. The horizontal line ( $E = 0$ ) is electron energy reference point (the energy of vacuum). Symbols  $E_c$  and  $E_v$  denote the bottom of the conduction band and the top of the valence band in  $\text{SiO}_x$ . The  $\text{SiO}_2$  bandgap is 8 eV [7]. Bandgap narrowing indicates a local increase in the silicon concentration in  $\text{SiO}_x$ . The least bandgap ( $E_g = 1.5$  eV) corresponds to the silicon phase. Thus, the maximum scale of potential fluctuations for electrons and holes is 2.6 and 3.8 eV, respectively. **Figure 10a** shows all possible versions of the  $\text{SiO}_x$  spatial structure. White, black, and gray colors correspond to  $\text{SiO}_2$ , a-Si, and silicon suboxides, respectively. If the silicon cluster size  $L$  is small, size quantization effects can be observed in it. Such a cluster is indicated in the figure by numeral 1. Numeral 2 indicates the macroscopic silicon cluster in silicon oxide. In this case, the intermediate layer of silicon suboxides is absent, and the Si/ $\text{SiO}_2$  interface in the

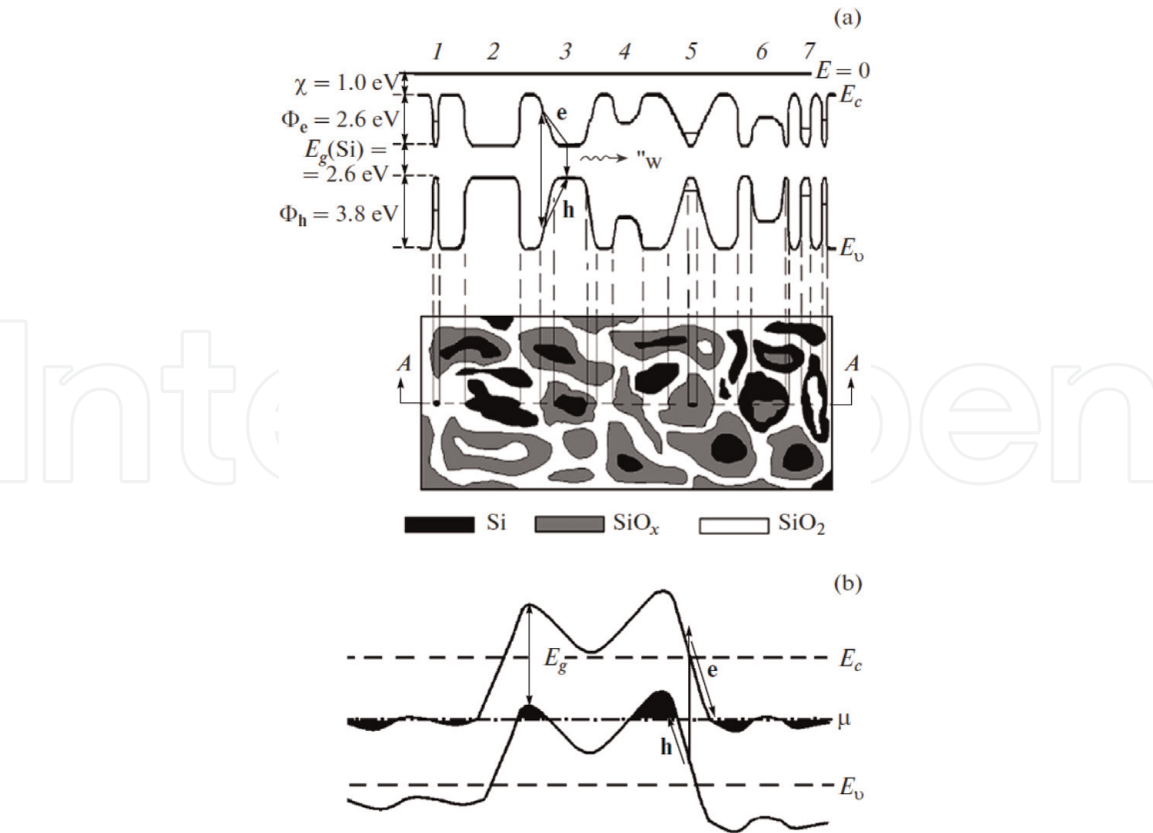


**Figure 10.**  
(a) IM model: the schematic two-dimensional pattern of the  $\text{SiO}_x$  structure and the  $\text{SiO}_x$  energy-level diagram for section A–A. White, black, and gray colors correspond to  $\text{SiO}_2$ ,  $\text{a-Si}$ , and silicon suboxides, respectively.  $\Phi_e$  and  $\Phi_h$  barriers for electrons and holes at the interface  $\text{a-Si/SiO}_2$ , respectively. (b) Model of potential fluctuation (Shklovskii-Efros model) in a heavily doped compensated semiconductor;  $\mu$  is the Fermi level.

energy-level diagram boundary is sharp. Numeral 3 indicates the silicon cluster surrounded by silicon suboxide. In this case, the  $\text{Si/SiO}_2$  interface in the energy-level diagram is shown by a smooth curve. Hereafter, it is assumed that the intermediate region (silicon suboxide) size significantly exceeds the  $\text{Si—O}$  and  $\text{Si—Si}$  bond length. Numeral 4 indicated the suboxide silicon cluster in  $\text{SiO}_2$ . Numeral 5 indicates the silicon cluster in silicon suboxide. Numeral 6 indicates the suboxide cluster in silicon, and numeral 7 indicates the  $\text{SiO}_2$  cluster in silicon.

The model of large-scale potential fluctuations (Shklovskii-Efros model) in a heavily doped compensated semiconductor was developed earlier (Figure 10b) [28]. In this model, the bandgap is constant, and potential fluctuations occur due to the nonuniform spatial distribution of the charged ionized donors and acceptors. An electron-hole pair excitation results in spatial separation of electrons and holes, which does not facilitate their recombination. The principal difference between the proposed model of nanoscale potential fluctuations in  $\text{SiO}_x$  and the Shklovskii-Efros model is as follows. Large-scale potential fluctuations in compensated semiconductors are of electrostatic nature associated with spatial fluctuations of the charge density of donors and acceptors. The bandgap is constant (Figure 10b), and the electric field caused by spatial potential fluctuations promotes electron and hole separation. In  $\text{SiO}_x$ , potential fluctuations are caused by local fluctuations of the chemical composition.

In the IM model, in contrast to the Shklovskii-Efros model, the space charge is absent. According to the IM model, local fluctuations in the  $\text{SiO}_x$  chemical composition result in spatial potential fluctuations which, in turn, lead to changes in local electric fields for electrons and holes. These fields at the same point of the  $\text{SiO}_x$  sample are different in magnitude and direction (Figure 10a). When an



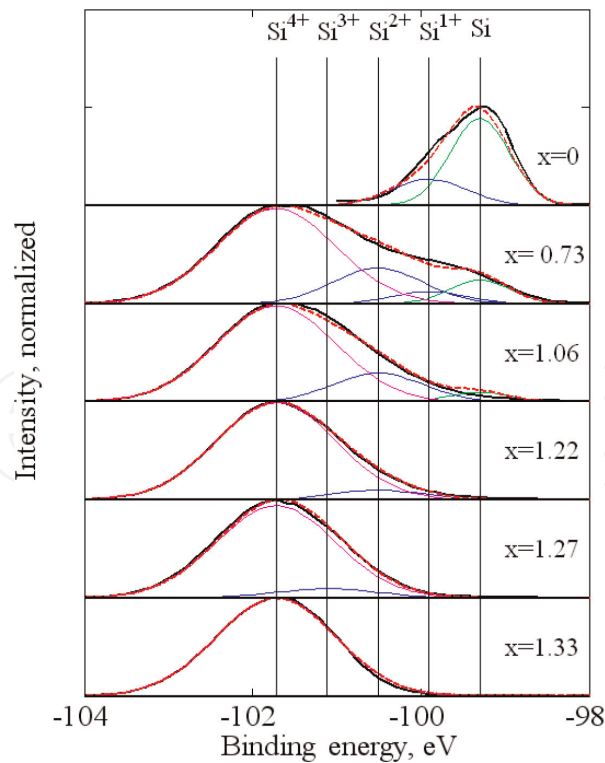


**Figure 11.** Experimental XPS spectra of the Si 2p level in  $\text{SiN}_x$  (solid black lines) and the results of theoretical modeling using the IM model (dashed red lines). Green line is peak from  $\text{Si}-\text{Si}_4$  tetrahedron, and magenta line is peak from  $\text{Si}-\text{N}_4$  tetrahedron.

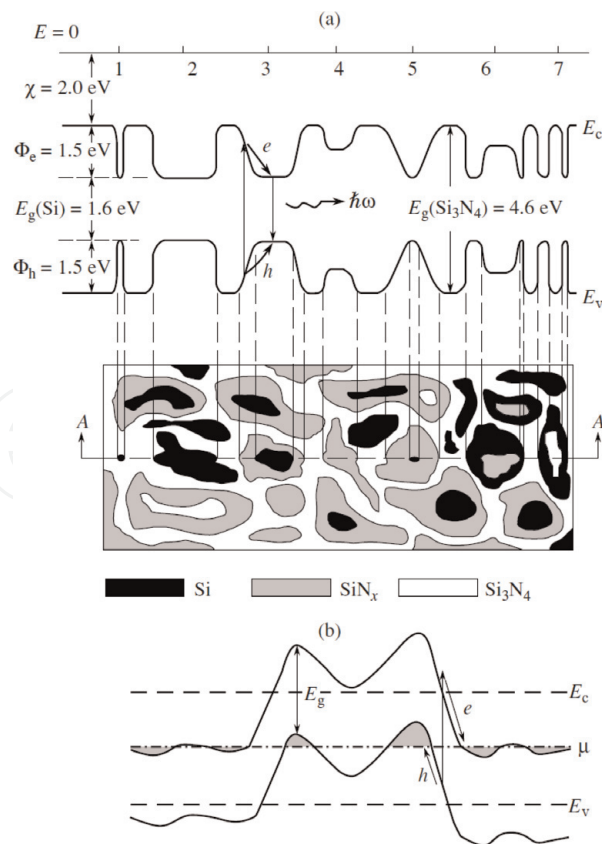


**Figure 12.** Schematic diagrams illustrating the proposed intermediate model of  $\text{SiN}_x$ : (a) a two-dimensional diagram of  $\text{SiN}_x$  structure showing (bottom) the regions of a silicon phase, stoichiometric silicon nitride, and subnitrides and (top) the energy band profile of  $\text{SiN}_x$  in the A-A section ( $E_c$  is the conduction band bottom;  $E_v$  is the valence band top;  $\Phi_e$  and  $\Phi_h$  are the energy barriers for electrons and holes at the a-Si- $\text{Si}_3\text{N}_4$  interfaces, respectively;  $E_g$  is the bandgap width). (b) The potential fluctuations in Shklovskii-Efros model.

electron-hole pair is excited in  $\text{SiO}_x$ , the electric field for electron and hole promotes (see in **Figure 10a**) their recombination. In the case of the radiative recombination mechanism,  $\text{SiO}_x$  is an efficient emitting medium. Nanoscale potential fluctuations in  $\text{SiO}_2$  promote electron and hole localization in potential wells (silicon clusters) [7]. This effect is used for developing the high-speed nonvolatile memory based on charge localization in  $\text{SiO}_x$  and can be used in memristors.

In the case of  $\text{SiN}_x$  films, the approach for determining the stoichiometric parameter  $x$  from XPS data analysis is similar, but unlike Eq. (12), the probability of finding the  $\text{SiN}_v\text{Si}_{(4-v)}$  tetrahedron (the fraction of given  $v$ -type tetrahedra), where  $v = 0, 1, 2, 3, 4$  in  $\text{SiN}_x$  for composition  $x$ , is given by

$$W_v^{RB}(v, x) = \frac{4!}{v!(4-v)!} \left(\frac{3x}{4}\right)^v \left(1 - \frac{3x}{4}\right)^{4-v} \quad (14)$$

Experimental XPS spectra are also not described by pure RB or RM models. However, good agreement between the experimental and calculated spectra is observed for IM model (**Figure 11**).

The nanoscale fluctuations of potential in  $\text{SiN}_x$  films (**Figure 12**) are also similar to nanoscale fluctuations of potential in  $\text{SiO}_x$ . In the case of  $\text{SiN}_x$  films, the IM is more adequate to describe the real structure and fluctuation of potential. In schematic picture in the bottom of **Figure 12**, one can see the possible appearance of such structures—Si core surrounded by  $\text{SiN}_x$  shell and  $\text{Si}_3\text{N}_4$  matrix. So, the proposed IM also can be called as core-shell-matrix model.

## 6. Memristor effects in $\text{SiO}_x$ films

Resistive random-access memory (RRAM) [29, 30] is the highly promising candidate for the next-generation nonvolatile memory (NVM), because conventional charge-based memories, namely, dynamic random-access memory and flash memory, have too low capacitance after continuously downscaling into 1X-nm regimes. In addition, an RRAM array can be fabricated in the back end of the line of a complementary metal-oxide-semiconductor circuit, which makes such device an excellent candidate for embedded NVM (e-NVM) application. The typical write speed of RRAM device ranges from 100 ns to 1  $\mu\text{s}$ , which is three to four orders of magnitude faster than flash memory. Such high-speed and process-compatible e-NVM can enable hardware technologies such as artificial intelligence and neuromorphic computing.

The conduction mechanism of RRAM, however, is not fully understood, and it is generally attributed to metallic filament conduction because of its metal-insulator-metal (MIM) structure, where the insulator is usually formed by metal oxide-based dielectric. The first RRAM that does not contain any metal in both the electrodes and dielectric insulator (nonmetal RRAM) is demonstrated here. To obtain RRAM device, a 15-nm-thick  $\text{SiO}_x$  was deposited directly on a  $\text{p}^+$ -Si substrate by reactive sputtering. Then, a 15-nm-thick amorphous  $\text{n}^+$ -Si layer was formed as the top junction electrode. The value  $x$  in  $\text{SiO}_x$  was determined to be 0.62. Because no metal or metallic ions were present in the whole RRAM device, metallic filaments were not formed.

**Figure 13(a)** depicts the measured  $I$ - $V$  characteristics of an  $\text{n}^+$ -Si/ $\text{SiO}_{0.62}$ / $\text{p}^+$ -Si RRAM device. During the forming step, the device was first subjected to a 6 V and 100  $\mu\text{A}$  compliance current stress to attain the LRS. The same device was reset into

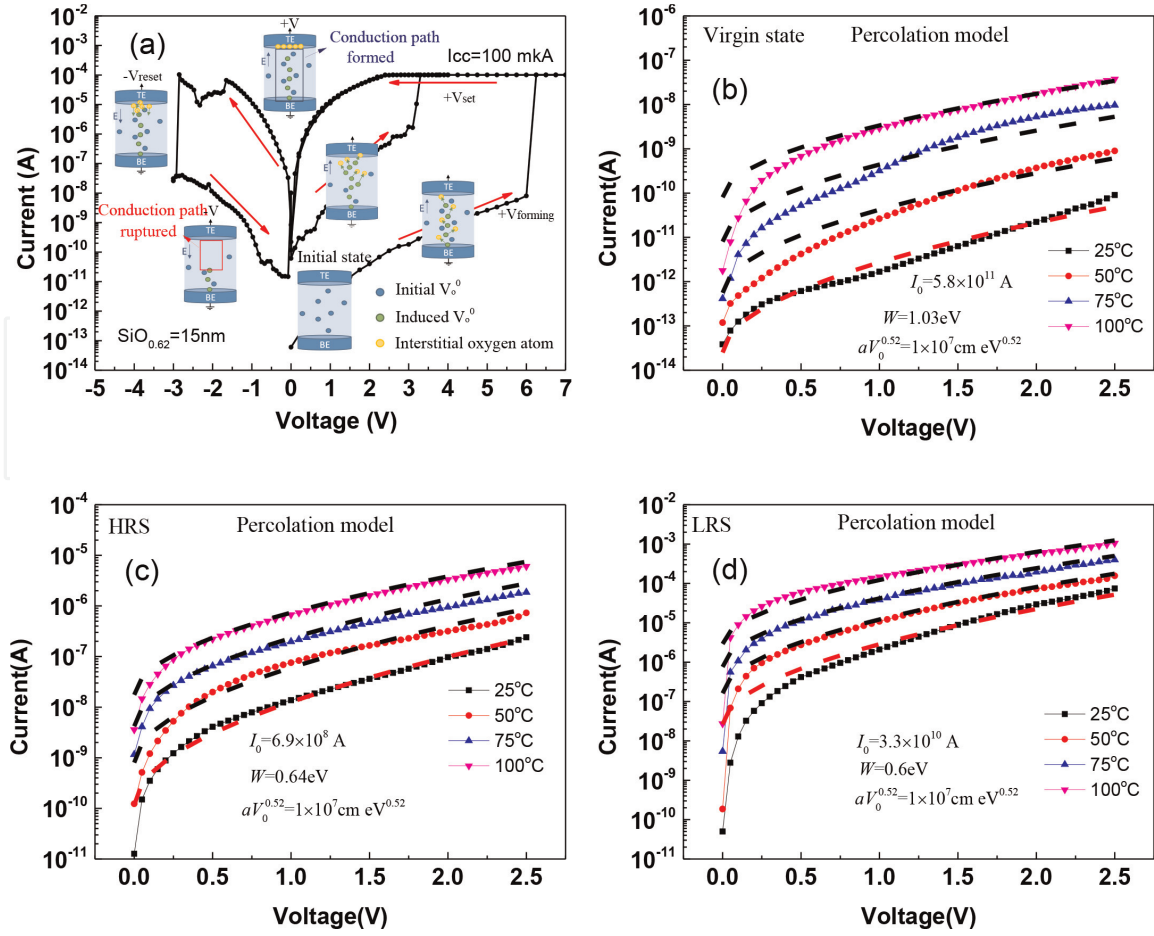


**Figure 13.**

(a)  $I$ - $V$  characteristics of  $n^+-\text{Si}/\text{SiO}_{0.62}/p^+-\text{Si}$  RRAM device under forming, set, and reset operations.  $I$ - $V$  dependences of (b) VS, (c) HRS, and LRS (d) currents of  $n^+-\text{Si}/\text{SiO}_x/p^+-\text{Si}$  RRAM and fitting curves of Shklovskii-Efros model.

HRS after a negative voltage bias. Then, the device was set to LRS again under a positive voltage bias. However, the positive set voltage was lower than the forming voltage once the RRAM switching function was established.

The current conduction mechanism is crucial for RRAM devices. To understand the conductive mechanism in this completely nonmetal RRAM, the measured  $I$ - $V$  curves at different temperatures were further analyzed. **Figure 13(b), (c), and (d)** depict the measured and modeled  $I$ - $V$  curves in the virgin state (VS), HRS, and LRS conditions, respectively. All state the HRS and LRS currents adhere to the Shklovskii-Efros percolation model [28]:

$$I = I_0 \exp \left( - \frac{W_e - (Ce \frac{U}{a} a V_0^\gamma)^{\frac{1}{1+\gamma}}}{kT} \right) \quad (15)$$

where  $I_0$ ,  $W_e$ ,  $a$ ,  $V_0$ ,  $C$ , and  $\gamma$  are the preexponential factor, percolation energy, space scale of fluctuations, energy fluctuation amplitude, numeric constant which is equal to 0.25, and critical index which is equal to 0.9, respectively. The simulation by the Shklovskii-Efros model gives reasonable model parameters to all resistance state (**Figure 13(b-d)**). The percolation energy decreases with decreasing resistance. The relation  $a \times V_0^{0.52} = 1 \times 10^{-7} \text{ cm eV}^{0.52}$  does not change from resistance to resistance. This is due to the fact that decreasing resistance increases space scale of fluctuations  $a$ , but decreases energy fluctuation amplitude  $V_0$ . In addition, it can be said that the Shklovskii-Efros percolation model is applicable to the LRS case,

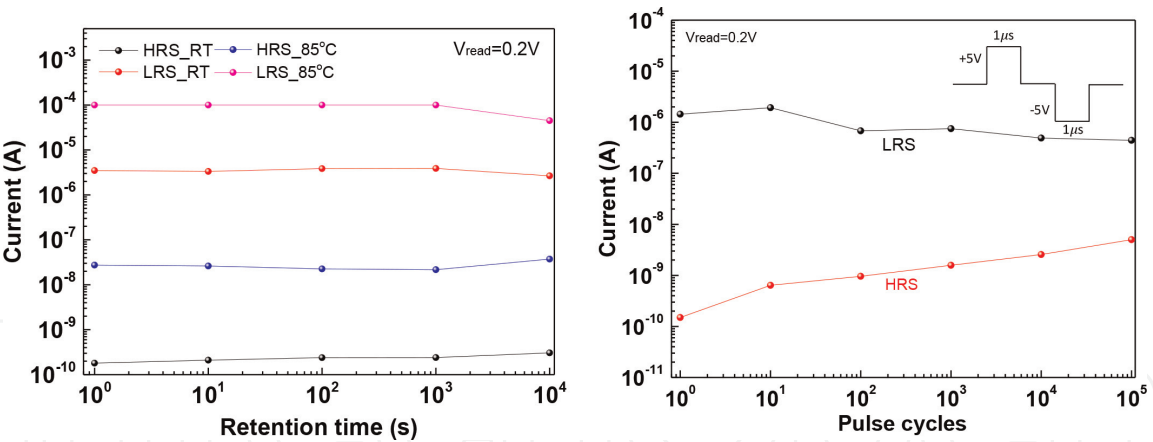


**Figure 14.**  
(left) Retention characteristics of  $n^+$ -Si/SiO<sub>0.62</sub>/p<sup>+</sup>-Si RRAM devices at RT and 85°C. (right) Endurance characteristics of  $n^+$ -Si/SiO<sub>0.62</sub>/p<sup>+</sup>-Si RRAM devices.

and then, it can be assumed that the conducting channel is not continuous. Hence, the simulated results demonstrate that the charge transport of the  $n^+$ -Si/SiO<sub>0.62</sub>/p<sup>+</sup>-Si RRAM in VS, HRS, and LRS are described by the Shklovskii-Efros percolation model.

**Figure 13(a)** plots potential switching mechanisms. During the forming step, the current is conducted through the initial  $\text{V}_\text{o}^{2+}$  inside the  $\text{SiO}_x$  layer [31]. When the RRAM device was under sufficiently high positive voltage, soft breakdown in  $\text{SiO}_x$  occurred and disrupted the covalent bonds [32], generating unbonded Si ions,  $\text{O}^{2-}$ , and  $\text{V}_\text{o}^{2+}$ . It is assumed that after generation of anti-Frenkel pairs, electrons are redistributed to maintain charge neutrality, and new oxygen vacancies ( $\text{V}_\text{o}^0$ ) and interstitial oxygen atoms are formed [30]. Because the atomic size of O is significantly smaller than Si, the interstitial oxygen atoms and  $\text{V}_\text{o}^0$  could migrate inside  $\text{SiO}_x$  under the applied electric field. At the end of the forming process, the interstitial oxygen atoms were attracted to the positive voltage and accumulated at the interface of top  $n^+$ -i junction. Once the conduction path was formed, electrons could transport through the  $\text{V}_\text{o}^0$ , creating the LRS current pass in the  $\text{SiO}_x$  layer. After application of a negative voltage, interstitial oxygen atoms moved away from the top  $n^+$ -i junction and recombined with  $\text{V}_\text{o}^0$  to rupture the conduction path—the reset process. After a positive voltage was applied again, the set process behaved as the forming process to form a conduction path, but under a lower positive voltage than the forming voltage due to not all generating in the forming process  $\text{V}_\text{o}^0$  recombined in the reset process.

Data retention and endurance are necessary characteristics for NVM, and they are related to the nonvolatile behavior and lifetime of an RRAM device. **Figure 14** (left) depicts the retention characteristics of the  $n^+$ -Si/SiO<sub>0.62</sub>/p<sup>+</sup>-Si RRAM device. The completely nonmetal RRAM device could achieve favorable retention with a slight resistive window decay from  $1.9 \times 10^4$  to  $8.7 \times 10^3$  at RT and  $3.6 \times 10^3$  to  $1.2 \times 10^3$  at 85°C after  $10^4$  s retention.

**Figure 14** (right) depicts the pulsed endurance of the  $n^+$ -Si/SiO<sub>0.62</sub>/p<sup>+</sup>-Si RRAM device under set/reset pulses of +5/−5 V for 1 μs. In this case, higher voltages were used than DC switching cases because the energy to disrupt the covalent  $\text{SiO}_x$  bonds equals to the multiplication of  $I$ ,  $V$ , and *time*. The resistance ratio between HRS and LRS decreased after increasing the pulsed cycles; however, the device exhibited excellent endurance with a resistance window of 89 after  $10^5$  pulsed switching cycles [33].



## 7. Conclusions

The silicon amorphous nanoclusters in as-deposited  $\text{SiO}_x$  and  $\text{SiN}_x$  films and silicon nanocrystals in the annealed films were studied using structural and optical methods. To analyze the sizes of silicon nanocrystals from the analysis of Raman scattering data, the phonon confinement model was refined.

From the analysis of XPS, Raman, and IR spectroscopy data, it has been established that pure random mixture and random bonding models do not adequately describe the real structure of the  $\text{SiO}_x$  and  $\text{SiN}_x$  films. The intermediate model was proposed. The nanoscale potential fluctuations in  $\text{SiO}_x$  and  $\text{SiN}_x$  films can be interpreted in the framework of the proposed model. The memristor effects in  $\text{SiO}_x$ -based nonmetal structures were demonstrated.

## Acknowledgements

The work was supported by the Russian Science Foundation (Project No. 18-49-08001) and the Ministry of Science and Technology (MOST) of Taiwan (No. 107-2923-E-009-001-MY3).

## Author details

Vladimir Volodin<sup>1,2\*</sup>, Vladimir Gritsenko<sup>1,2,3</sup>, Andrei Gismatulin<sup>1</sup> and Albert Chin<sup>4</sup>

<sup>1</sup> Rzhanov Institute of Semiconductor Physics SB RAS, Novosibirsk, Russia


<sup>2</sup> Novosibirsk State University, Novosibirsk, Russia

<sup>3</sup> Novosibirsk State Technical University, Novosibirsk, Russia

<sup>4</sup> National Chiao Tung University, Hsinchu, Taiwan, ROC

\*Address all correspondence to: volodin@isp.nsc.ru

## IntechOpen

© 2019 The Author(s). Licensee IntechOpen. This chapter is distributed under the terms of the Creative Commons Attribution License (<http://creativecommons.org/licenses/by/3.0>), which permits unrestricted use, distribution, and reproduction in any medium, provided the original work is properly cited. 

## References

- [1] Pavese L, Turan R, editors. *Silicon Nanocrystals Fundamentals, Synthesis and Applications*. Germany: Wiley; 2010. p. 652. ISBN: 978-3-527-32160-5
- [2] Greben M, Khoroshyy P, Liu X, Pi X, Valenta J. Fully radiative relaxation of silicon nanocrystals in colloidal ensemble revealed by advanced treatment of decay kinetics. *Journal of Applied Physics*. 2017;**122**:034304. DOI: 10.1063/1.4993584
- [3] Sychugov I, Juhasz R, Valenta J, Linnros J. Narrow luminescence linewidth of a silicon quantum dot. *Physical Review Letters*. 2005;**94**: 087405. DOI: 10.1103/PhysRevLett.94.087405
- [4] Park N-M, Kim T-S, Park S-J. Band gap engineering of amorphous silicon quantum dots for light-emitting diodes. *Applied Physics Letters*. 2001;**78**:2575-2577. DOI: 10.1063/1.1367277
- [5] Anutgan T, Anutgan M, Atilgan I, Katircioglu B. Electroformed silicon nitride based light emitting memory device. *Applied Physics Letters*. 2017;**111**:053502. DOI: 10.1063/1.4997029
- [6] Gismatulin AA, Kruchinin VN, Gritsenko VA, Prosvirin IP, Yen T-J, Chin A. Charge transport mechanism of high-resistive state in RRAM based on SiO<sub>x</sub>. *Applied Physics Letters*. 2019;**114**: 033503. DOI: 10.1063/1.5074116
- [7] Gritsenko VA. Atomic structure of amorphous nonstoichiometric silicon oxides and nitrides. *Physics-Uspekhi*. 2008;**178**:699-708. DOI: 10.1070/PU2008v051n07ABEH006592
- [8] Smith JE Jr, Brodsky MH, Crowder BI, Nathan MI. Raman spectra of amorphous Si and related tetrahedrally bonded semiconductors. *Physical Review Letters*. 1971;**26**:642-646. DOI: 10.1103/PhysRevLett.26.642
- [9] Parker JH Jr, Feldman DW, Ashkin M. Raman scattering by silicon and germanium. *Physical Review*. 1967;**155**: 712-714. DOI: 10.1103/PhysRev.155.712
- [10] Bustarret E, Hachicha MA, Brunel M. Experimental determination of the nanocrystalline volume fraction in silicon thin films from Raman spectroscopy. *Applied Physics Letters*. 1988;**52**:1675-1677. DOI: 10.1063/1.99054
- [11] Zhigunov DM, Kamaev GN, Kashkarov PK, Volodin VA. On Raman scattering cross section ratio of crystalline and microcrystalline to amorphous silicon. *Applied Physics Letters*. 2018;**113**:023101. DOI: 10.1063/1.5037008
- [12] Richter H, Wang ZP, Lay L. The one phonon Raman spectrum of microcrystalline silicon. *Solid State Communications*. 1981;**39**:625-629. DOI: 10.1016/0038-1098(81)90337-9
- [13] Pailard V, Puech P, Laguna MA, Carles R, Kohn B, Huysen F. Improved one-phonon confinement model for an accurate size determination of silicon nanocrystals. *Journal of Applied Physics*. 1999;**86**:1921-1924. DOI: 10.1063/1.370988
- [14] Volodin VA, Sachkov VA. Improved model of optical phonon confinement in silicon nanocrystals. *Journal of Experimental and Theoretical Physics*. 2013;**116**:87-94. DOI: 10.1134/S1063776112130183
- [15] Cardona M, Günterodt G, editors. *Light Scattering in Solids II. Basic Concept and Instrumentation*. Berlin: Springer-Verlag; 1982. p. 251. ISBN: 3-540-11380-0

- [16] Cheng W, Ren S-F. Calculations on the size effects of Raman intensities of silicon quantum dots. *Physical Review B*. 2002;**65**:205305. DOI: 10.1103/PhysRevB.65.205305
- [17] Keating PN. Effect of invariance requirements on the elastic strain energy of crystals with application to the diamond structure. *Physics Review*. 1966;**145**:637-645. DOI: 10.1103/PhysRev.145.637
- [18] Dolling G. Lattice vibrations in crystals with the diamond structure. In: *Inelastic Scattering of Neutrons in Solids and Liquids: II. Proceedings of IAEA, Vienna*. 1963. pp. 37-48
- [19] Kulda J, Strauch D, Pavone P, Ishii Y. Inelastic-neutron-scattering study of phonon eigenvectors and frequencies in Si. *Physical Review B*. 1994;**50**:13347-13356. DOI: 10.1103/PhysRevB.50.13347
- [20] Kirk CT. Quantitative analysis of the effect of disorder-induced mode coupling on infrared absorption in silica. *Physical Review B*. 1988;**38**:1255-1273. DOI: 10.1103/PhysRevB.38.1255
- [21] Pai PG, Chao SS, Takagi Y, Lucovsky G. Infrared spectroscopic study of SiO<sub>x</sub> films produced by plasma enhanced chemical vapor deposition. *Journal of Vacuum Science and Technology A*. 1986;**4**:689-694. DOI: 10.1116/1.573833
- [22] Yin Z, Smith FW. Optical dielectric function and infrared absorption of hydrogenated amorphous silicon nitride films: Experimental results and effective-medium-approximation analysis. *Physical Review B*. 1990;**42**:3666-3675. DOI: 10.1103/PhysRevB.42.3666
- [23] Korchagina TT, Marin DV, Volodin VA, Popov AA, Vergnat M. Structure and optical properties of SiN<sub>x</sub>: H films with Si nanoclusters produced by low frequency plasma enhanced chemical vapor deposition. *Semiconductors*. 2009;**43**:1514-1520. DOI: 10.1134/S1063782609110207
- [24] Volodin VA, Bugaev KO, Gutakovsky AK, Fedina LI, Neklyudova MA, Latyshev AV, et al. Evolution of silicon nanoclusters and hydrogen in SiN<sub>x</sub>:H films: Influence of high hydrostatic pressure under annealing. *Thin Solid Films*. 2012;**520**:6207-6214. DOI: 10.1016/j.tsf.2012.05.019
- [25] Gritsenko VA, Xu JB, Kwok RWM, Ng YN, Wilson IH. Short range order and the nature of defects and traps in amorphous silicon oxynitride governed by the Mott rule. *Physical Review Letters*. 1998;**81**:1054-1057. DOI: 10.1103/PhysRevLett.81.1054
- [26] Bell FG, Ley L. Photoemission study of SiO<sub>x</sub> (0 ≤ x ≤ 2) alloys. *Physical Review B*. 1988;**37**:8383-8393. DOI: 10.1103/PhysRevB.37.8383
- [27] Hickmott TW, Baglin JE. Stoichiometry and atomic defects in rf-sputtered SiO<sub>2</sub>. *Journal of Applied Physics*. 1979;**50**:317-323. DOI: 10.1063/1.325662
- [28] Shklovskii BI, Efros AL. *Electronic Properties of Doped Semiconductors*. Heidelberg: Springer; 1984. p. 416
- [29] Strukov DB, Snider GS, Stewart DR, Williams RS. The missing memristor found. *Nature*. 2008;**453**:80-83. DOI: 10.1038/nature06932
- [30] Mehonic A, Shluger AL, Gao D, Valov I, Miranda E, Ielmini D, et al. Silicon oxide (SiO<sub>x</sub>): A promising material for resistance switching? *Advanced Materials*. 2018;**30**:1801187. DOI: 10.1002/adma.201801187
- [31] Dong LP, Jia RX, Xin B, Peng B, Zhang YM. Effects of oxygen vacancies

on the structural and optical properties  
of  $\beta$ -Ga<sub>2</sub>O<sub>3</sub>. Scientific Reports. 2017;7:  
40160. DOI: 10.1038/srep40160

[32] Padovani A, Gao DZ, Shluger AL,  
Larcher L. A microscopic mechanism of  
dielectric breakdown in SiO<sub>2</sub> films: An  
insight from multi-scale modeling.  
Journal of Applied Physics. 2017;121:  
155101. DOI: 10.1063/1.4979915

[33] Te JY, Gismatulin A, Volodin V,  
Gritsenko V, Chin A. Novel all nonmetal  
resistive random access memory.  
Scientific Reports. 2019;9(1):6144.  
DOI: 10.1038/s41598-019-42706-9